# Molecular Dynamics Simulation of Mechanical Behavior of Nanoporous Copper Foams

by

Charles Cantrell

Submitted to the Department of Material Science and Engineering
in Partial Fulfillment of the Requirements for the Degree of
Bachelor of Science in Material Science and Engineering

at the

Massachusetts Institute of Technology
[June 2006]
May 2006

Signature of Author: ..............................................................
Department of Material Science and Engineering
May 26, 2006

Certified by: ..............................................................
Sidney Yip
Professor of Nuclear Science and Engineering and Materials Science and Engineering
Thesis Supervisor

Accepted by: ..............................................................
Caroline A. Ross
Professor of Materials Science and Engineering
Chair, Departmental Undergraduate Committee

# Molecular Dynamics Simulation of Mechanical Behavior of Nanoporous Copper Foams

by

Charles Cantrell

Submitted to the Department of Material Science and Engineering
in Partial Fulfillment of the Requirements for the Degree of
Bachelor of Science in Material Science and Engineering

## ABSTRACT

Metallic foams have a variety of unique mechanical properties that make them prime candidates for many different applications. Recent developments in manufacturing have allowed for the creation of nanoporous foams but still relatively little is known about foam behavior on the nano-scale. To determine if macro-scale metallic foam theory scaled appropriately to nanoporous foams, the mechanical behavior of nanoporous copper was simulated. Molecular dynamics (MD) simulations were performed at room temperature using the Mishin potential on tetrakaidecahedron foam structures. In closed-celled foams close agreement is observed between simulated Young's moduli and constitutive theory. Nanoporous closed-celled foams also show mechanical failure mechanisms similar to those seen on the macro-scale.

Thesis Supervisor: Sidney Yip

Title: Professor of Nuclear Science and Engineering and Materials Science and Engineering

# TABLE OF CONTENTS

# LIST OF FIGURES

**Figure 18** Series of figures representing the continuum properties of a metal foam under tension. At point a.) elastic regime, b.) localization of strain, c.) breaking of strut, d.) full fracture of strut, e.) and f.) fusion of two struts.

**Figure 19** Series of figures representing the continuum properties of a metal foam under compression. At point a.) elastic regime, b.) onset of plastic deformation, c.) collapse of pore, d.) propagation of collapsing pore, e.) approaching full compression.

# Chapter 1

# Introduction

Until recently, metallic foams were characterized by high costs and relatively poor qualities (non-uniform cellular structure, large voids, etc.). In the past few years, however, new processing methods have increased the quality and production rates of these foams, and consequently, interest in them has skyrocketed [Gibson 2000, Gioux 2000]. More importantly to this paper, recent production techniques, such as electrochemically dealloying or electrolytic dissolution, have allowed for the creation of nanoporous metallic foams [Biener 2005a, Biener 2005b].

Macro-scale metallic foams have numerous beneficial properties that allow for many possible applications. First, because of their high strength to weight ratio, metallic foams have been used as in-body implants to promote bone growth [Zhu 1997]. Metallic foams also have unique thermal insulation properties, which is why NASA is currently investigating the use of metallic foams as heat shields for their space shuttle re-entry [Palmer 1997]. In addition, metallic foams have mechanical properties which allow them to be used in energy absorbing devices [Gioux 2000]. Nanoporous foams, specifically, have attracted interest due to their potential sensor and actuator applications [Biener 2005].

There are two types of metallic foams, which have drastically different mechanical properties: open and closed celled. Because of their different mechanical behavior they are used in different applications. Closed-celled foams are able undergo large strains (up to about 60–70%) at almost constant stress making them great candidates for energy dissipation applications [Gibson 2000]. Open-celled foams have high thermal conductivity and the interconnectivity of voids, which allows gas to pass from one pore to another easily, making them useful in heat dissipation applications [Gibson 2000].

Significant experimental and theoretical work has been performed to characterize the mechanical behavior of macro-scale metallic foams [Gibson 2000, Andrews 2002, Andrews 1999, Gioux 2000, Han 2004, Onck 2005]. However, because of their recent development, far less research has been performed to determine the mechanical behavior of nano-scale foams [Biener 2005a, Biener 2005b], and consequently, no well developed theory exists. Furthermore, since constitutive macro-scale theory often breaks down at small scales, i.e. Hall-Petch, the well-defined macro-scale theories must be tested at the nano-scale before they can be applied.

This paper examines the mechanical behavior of nanoporous copper foams. Because of well-defined constitutive theory, we study the yield stress and Young's modulus of our foams. We will show that these foams behave according to current macro-scale theory. We discuss the effects of porosity and configuration (open vs. closed) on the mechanical behavior and compare it to current constitutive theory. Several important discrepancies between theory and simulated data exist and are discussed at length.

# Chapter 2

## Background

### 2.1) Types and Mechanical Properties of Foams

Foams are typically described as either open- or closed-celled. The difference between the two has to do with the interconnectivity of the pores. An open-celled foam, shown in Figure 1, is characterized by the interconnectivity of pores and is formed by the connection of struts where the faces between pores are "open" allowing air to pass from one pore to the next. Closed-celled foams, shown in Figure 2, do not have interconnected pores and are characterized by the faces or plates that separate the pores. The plates effectively "close" the pores preventing the air from passing easily from one pore to another. When deformed the dynamics of the air play an important role in the over-all mechanical behavior of these foams. If the air is not allowed to move freely it acts against the stress and provides additional mechanical support [Gibson 2000].

The single most important structural feature that affects the mechanical properties of foams is its relative density. The relative density is the ratio of the density of the foam to that of the solid. For foams, the relative density generally falls between 0.003 and 0.3 [Gibson 2000].

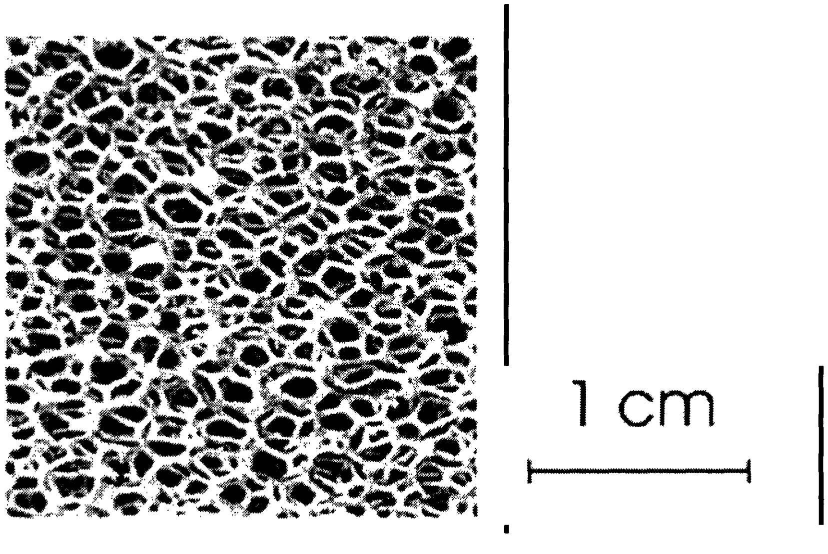

**Figure 1** Micrograph of an open-celled metallic foam. The open faces between pores allow for easy transfer of enclosed air. Reproduced from Gibson, 2000

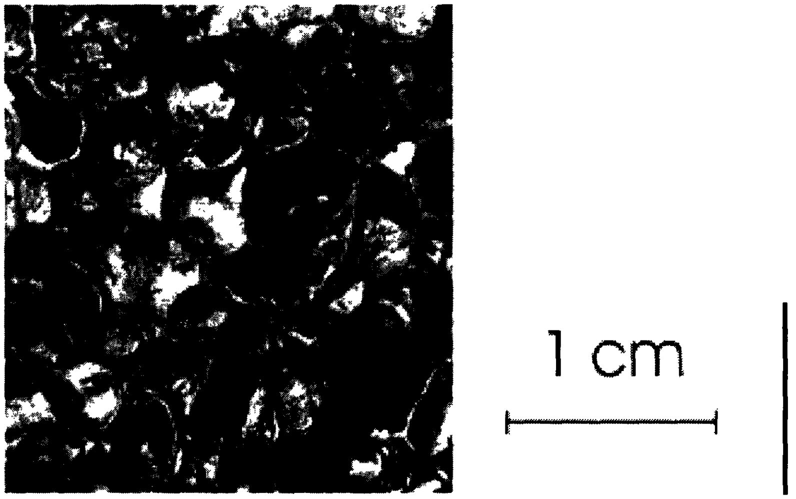

**Figure 2** Micrograph of a closed-celled metallic foam. The closed faces between the pores characterizes closed-celled foams. Reproduced from Gibson, 2000

### 2.1.1) Mechanical properties of open-celled foams

Current theory for open-celled metallic foams states the yield stress can be estimated using

$$\frac{\sigma_{y,foam}}{\sigma_{y,solid}} = C_1 \rho_{rel}^{1.5} \qquad (1)$$

where $\sigma_{y,foam}$ is the yield stress for the foam, $\sigma_{y,solid}$ is the yield stress for the solid, $\rho_{rel}$ is relative density and empirical data from many different foams suggests $C_1 \sim 0.3$ [Gibson 2000].

The Young's modulus relation behaves similarly,

$$\frac{E_{foam}}{E_{solid}} = C_2 \rho_{rel}{}^2 \qquad (2)$$

where $E_{foam}$ is the Young's modulus for the foam, $E_{solid}$ is the Young's modulus for the solid and $C_2 \sim 1$.

### 2.1.2) Mechanical properties of closed-celled foams

Closed-celled mechanical properties are very similar to those of open-celled foams. The slight difference is caused by the entrapment of the air in the pores and the bending of the faces between the pores. These differences results in an extra term in the yield stress and Young's modulus equations. Current theory for closed-celled metallic foams states the yield stress can be estimated using,

$$\frac{\sigma_{y,foam}}{\sigma_{y,solid}} = (C_3 \rho_{rel}^{1.5} + C_4 \rho_{rel}) \qquad (3)$$

where empirical data suggests $C_3 \sim .33$ and $C_4 \sim .44$ [Gibson 2000]. Unlike the open-celled foam, at relatively low densities the second term dominates and the above equation becomes quasi-linear.

Similar behavior occurs for the Young's modulus

$$\frac{E_{foam}}{E_{solid}} = (C_5 \rho_{rel}^{\ 2} + C_6 \rho_{rel}) \tag{4}$$

where analysis suggests $C_5 \sim C_6 \sim .32$.

## 2.2) Tetrakaidecahedron

A tetrakaidecahedron is a 14-sided figure composed of 8 regular hexagons and 6 squares and is created by truncating a regular octahedron [Zhu 1997]. A tetrakaidecahedron is formed when six square pyramids are removed from the corners of a regular octahedron. Figure 3, taken from Zhu [1996], shows tetrakaidecahedra filling space. Our recreation a tetrakaidecahedron on the molecular scale is shown in Figure 4.

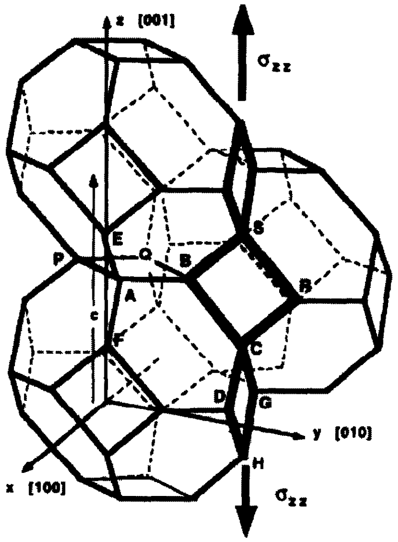

**Figure 3** Schematic of 3 tetrakaidecahedron. Notice the lower two produce a translationally space filling object. Reproduced from [Zhu 1996].

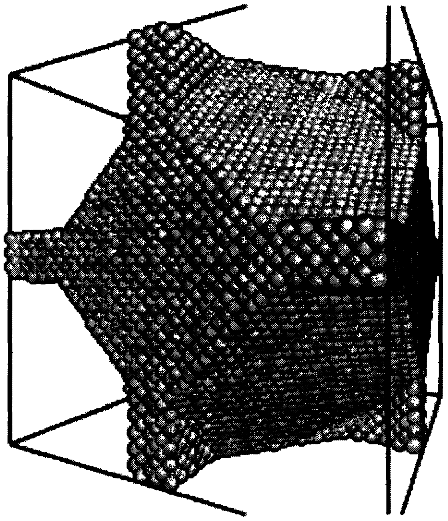

**Figure 4** Atomistic representation of the tetrakaidecahedron foam. Two tetrakaidecahedra are removed from an FCC crystal. The above unit is space filling along the X, Y and Z

Because the tetrakaidecahedron is created by removing 6 square pyramids from a regular octahedron, the volume of the tetrakaidecahedron is given by the volume of the octahedron minus six times the volume of the square pyramids, therefore the volume is

$$V = 8\sqrt{2}a^3 \tag{5}$$

From a similar process we see the surface area of a tetrakaidecahedron is given by

$$S = (6 + 12\sqrt{3})a^2 \tag{6}$$

The distances from the middle of the solid to the centers of the hexagonal and square faces are given by

$$r6 = \frac{\sqrt{6}}{2}a \tag{7}$$

$$r4 = \sqrt{2}a \tag{8}$$

respectively, where *a* is the length of the edges. The volume and surface area of the tetrakaidecahedron are important when determining the density and porosity of resulting foams and the distances from the centroid of the solid to the centers of the surfaces are used in the creation of the foams, described in the methods section.

## 2.3) Potentials

The potential energy, V, between any pair of atoms and is a function of the distance between them, r. The force on the atom can be calculated using the following relation

$$f(r) = -grad[V(r)] \tag{9}$$

where f(r) is the force. Knowing the force allows us to determine the future positions and velocities of the atoms.

### 2.3.1) Lennard-Jones Potential

The Lennard-Jones potential is a mathematical representation of the potential energy between two hard-sphere atoms. Any pair of atoms are subject to 2 distinct forces attracting and repelling them. At large distances, the two atoms are attracted by Van der Waals forces and when close together the two atoms repel one another due to electron cloud interactions. The Lennard-Jones potential takes into account these two distinct forces. The resulting potential is shown below

$$V(r) = 4\varepsilon\left[\left(\frac{\sigma}{r}\right)^{12} - \left(\frac{\sigma}{r}\right)^{6}\right] \qquad (10)$$

where ε is the well depth and σ is the hard sphere diameter. These two constants are distinct to the type of material being modeled, and thus V is a function of only r.

The positive term (and the 12th power) represents the repulsive potential and the negative term represents the attractive force. The competition between the opposing forces results in a minimum energy state and a static equilibrium atomic spacing. When fit using the proper constants the Lennard-Jones potential fits fairly well to empirical data, shown in Figure 5.

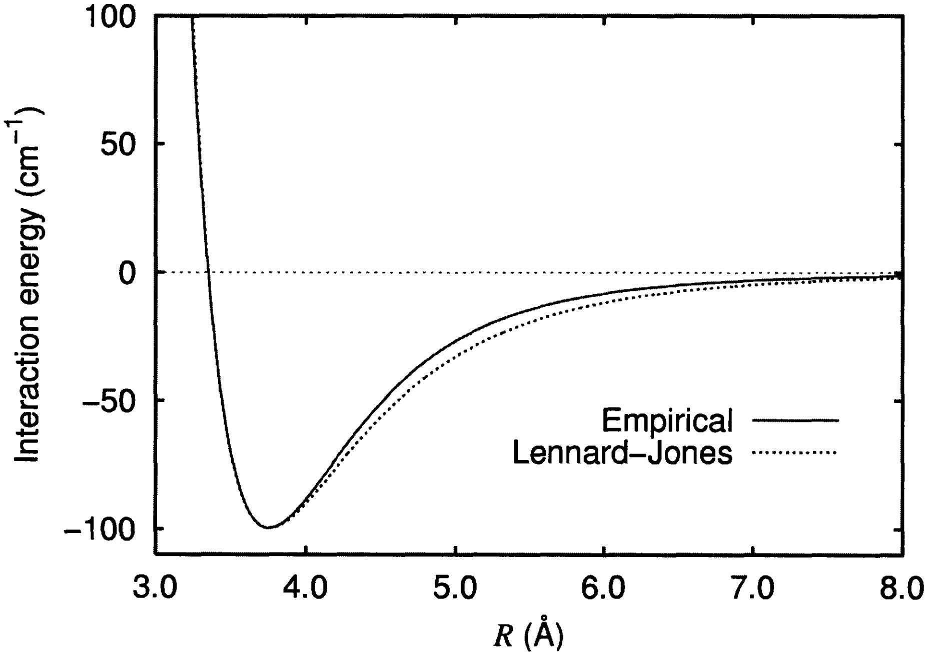

**Figure 5** Graph showing the Lennard-Jones potential versus experimental data. Graph taken from http://en.wikipedia.org/wiki/Lennard-Jones_potential

### 2.2.2) Mishin Potential

The Mishin potential is a specific potential based on the Embedded Atom Method (EAM), which assumes metals to be embedded in a cloud of electrons. Standard EAM potentials have the form

$$E = \sum_i G_i\left(\sum_{j \neq i} \rho_j(r_{ij})\right) + \frac{1}{2}\sum_{i \neq j} V(r_{ij}) \tag{11}$$

where the first term accounts for pair-wise atomic interaction and the second term accounts for the local electron density. $G_i$ is the embedding function, $\rho_j$ is the electron density as a function of the neighboring atoms, and $V(r_{ij})$ is the potential between a pair of atoms. The Mishin potential fits both terms to a database generated by Density Functional Theory (DFT) calculations. For Copper, the Mishin potential has been shown to be more accurate than the Lennard-Jones potential [Boyer 2004].

### 2.4.) Molecular Dynamics

Molecular dynamics (MD) simulations begin with a starting configuration containing the initial positions and velocities of all N atoms. To find the trajectories, Newton's equation of motion

$$F = ma, \tag{12}$$

where F is the force acting on the particle, m is the mass, and a is the acceleration, must be solved for each atom. The force is determined using the specified potential, and since the mass of the atom is known, we are able to determine each atom's acceleration. With the acceleration and current velocity and position, it is straight forward to determine the position of the atom at time t + Δt. This process is continued for a specified number of time steps, outputting information about the system at appropriate intervals [Yip 2002].

This procedure can be summed into the following algorithm:

1. The initial positions and velocities of each atom are specified in a starting configuration.
2. Using the potential, forces on each atom are calculated.
3. Using the calculated force and the current position and velocity, the atomic positions and velocities at time t + Δt are calculated
4. Move atoms forward in time by time step Δt
5. Steps 2 through 4 are repeated for a specified number of time steps.

MD simulations are bounded by two important parameters: the time step and the temperature. Choosing the appropriate time step is vital to the simulations, since each step costs computational time. A time step that is too short requires a longer simulation, and if the time step is too long, important information about atomic vibrations is lost, invalidating the simulation. The temperature of an MD simulation is important as well. MD simulations do not generically hold temperature constant. In order to hold temperature constant a thermostat must be used. A common thermostat method is velocity rescaling. Since temperature is directly related to the kinetic energy of the system, if the average velocity changes so does the temperature. Therefore, to hold the temperature constant, the velocities need to be rescaled to maintain the same average velocity.

### 2.4) Stress-Strain Curves

When performing mechanical deformation of any kind, the stress-strain curve is an important piece of information that can be gathered. From the stress-strain curve a variety of properties can be determined, including the Young's modulus and the yield stress. The theoretical stress-strain curves for metallic foams under uniaxial stress in both tension and compression are shown. The two stress-strain curves are slightly different but both have several important features that require discussion.

### 2.5.1) Tension

Under uniaxial tension the typical stress-strain curve for a metallic foam has five points of interest shown in the schematic in Figure 6 [Gibson 2000]. At point *(a.)* the structure is still undergoing elastic deformation, where the strain is evenly distributed throughout the structure. Point *(b.)* represents the onset of plastic deformation which usually occurs as a result of the movement of dislocations. At *(c.)* a crack has nucleated reducing stress. Though the nucleation of a crack creates surfaces it relieves much of the stress in the system by allowing atomic relaxation. The plateau region, shown as point *(d.)*, is caused as the crack propagates through the structure. Finally point *(e.)* occurs when the crack has fully propagated through the structure and sample is fully fractured. The fully fractured material will be in a zero stress state.

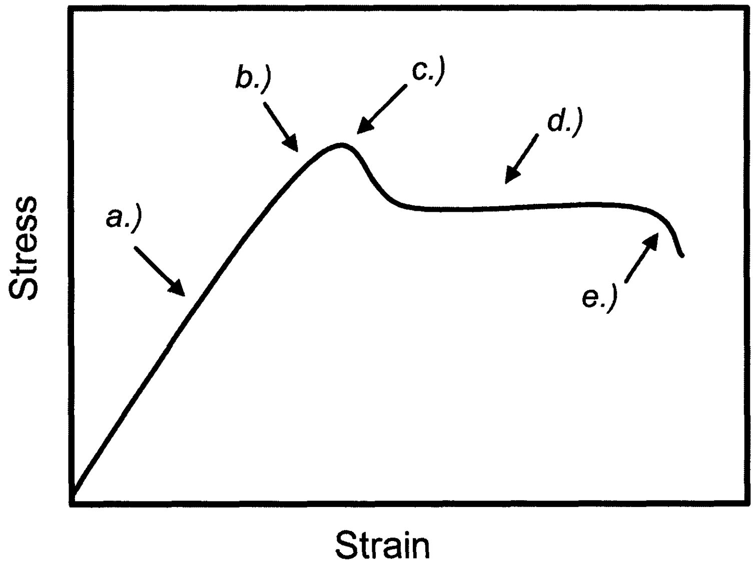

**Figure 6** Schematic of a typical stress v. strain curve for a metallic foam under uniaxial tension. a.) elastic regime, b.) onset of plastic deformation, c.) nucleation of crack, d.) crack propagation, e.) full fracture

### 2.5.2.) Compression

Under uniaxial compression the typical stress-strain curve for a metallic foam looks like the schematic Figure 7 [Gibson 2000]. As before, there are five points of interest shown in the compression stress-strain graph. The first four are essentially the same except that *(c.)* and *(d.)* represent the onset and propagation of collapsing pores instead of a crack. And finally point *(e.)* represents the regime where the structure is fully dense and resumes loading in compression, and as a result, the stress increases exponentially.

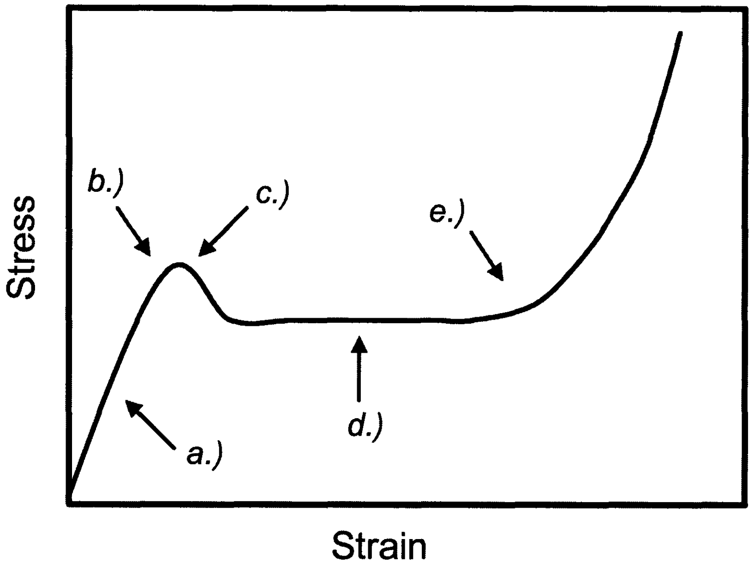

**Figure 7** Schematic of a typical stress v. strain curve for a metallic foam under uniaxial tension. a.) elastic regime, b.) onset of plastic deformation, c.) collapse of pore, d.) collapse propagation, e.) FCC compression regime

# Chapter 3

## Methods

The compressive and tensile mechanical behavior of nano-porous copper foams was tested using MD simulation. Tests were performed on open and closed celled foams created from a Face Centered Cubic (FCC) perfect crystal. Foams were produced using a tetrakaidecahedron structure and then allowed to relax to reduce their energy. The resulting foam configurations were deformed at a constant strain rate of $10^9$. Energy, deformation, and temperature information were output at every time step and the location of each individual atom was output every 2000 time steps. Foams were deformed for approximately 200,000 time steps representing 2 pico-seconds. All simulations were performed at a constant temperature of 300° K using velocity rescaling and the Mishin potential.

Different foams were tested to determine the effects of relative density, convergence and configuration (open vs. closed) on the mechanical behavior of nano-porous copper foams. To test the effects of relative density, 5 different closed-celled foams and 5 different open-celled foams were tested ranging the relative densities from 0.14 to 0.37.

Our foams were produced from an FCC perfect crystal so we first needed to create an FCC lattice. In order to do this, we created an FCC unit cell (which consists of 4 atoms) and repeated it along the X, Y, and Z axes to create a crystalline structure with the FCC cell as its basic building block. From this structure we remove unwanted cells to create our tetrakaidecahedron unit cell. We then repeat this unit cell along the X, Y, and Z axes to create our desired tetrakaidecahedron foam. The tetrakaidecahedron unit cell, pictured in Figure 4, is a set of two tetrakaidecahedra that are space filling when repeated along X, Y and Z axes. We translate the tetrakaidecahedron unit cell along the X, Y, and Z axes and we get our structure. This is shown in Figure 5.

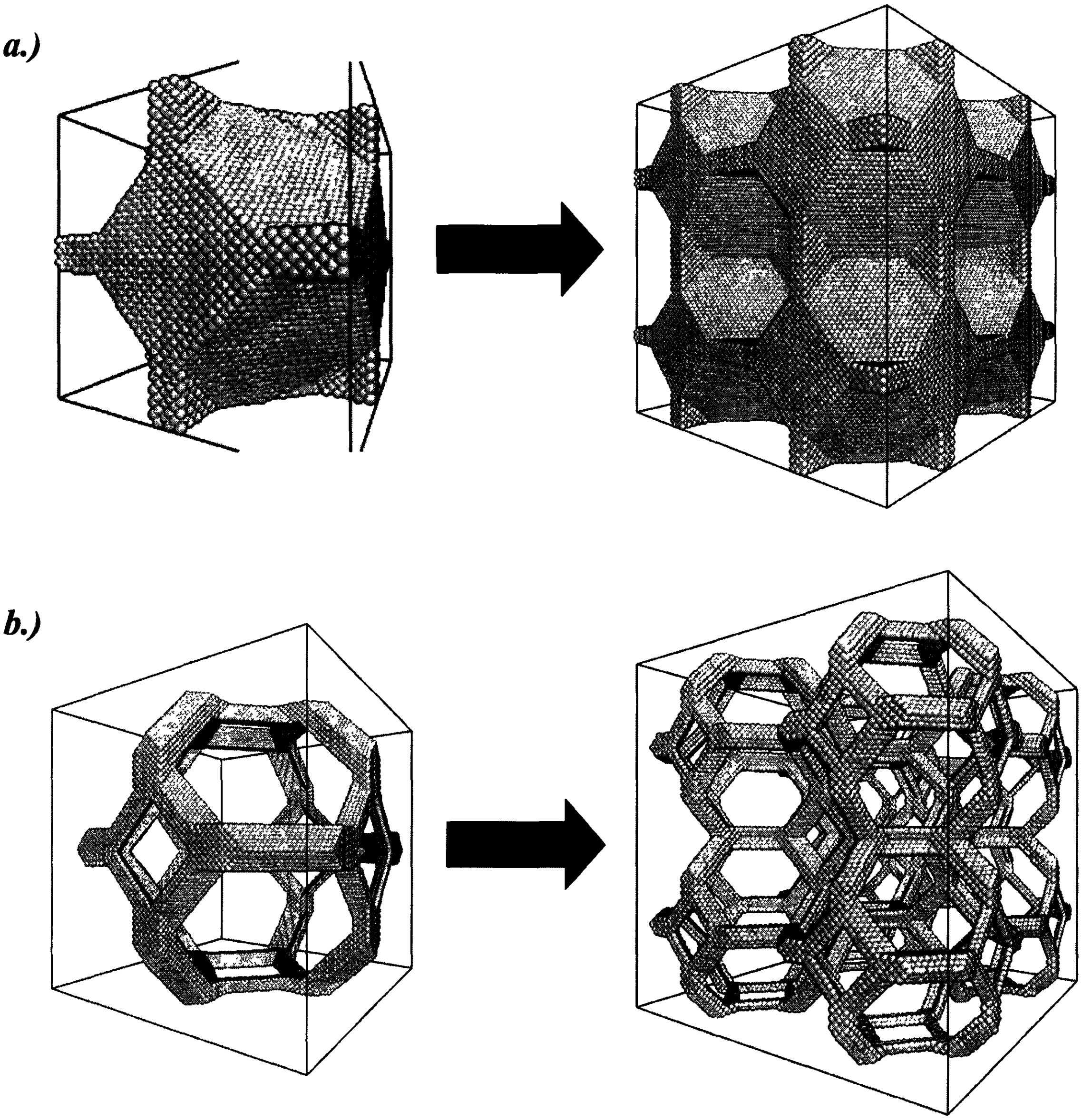

**Figure 8** An atomistic representation of the tetrakaidecahron unit cell and its translation to form initial configuration structures. *a.)* Closed-Cell *b.)* Open-Celled

To produce the tetrakaidecahedron unit cell, we start by placing the center of a tetrakaidecahedron at the origin of the FCC cell. We loop over all particles checking if they are located inside the tetrakaidecahedron. The atoms whose centers fell within this volume are "flagged" and later taken out of the structure. Next we translate the center of the tetrakaidecahedron through a hexagonal face by $2r6+t$ where t is the thickness of the strut and r6, given by Equation 7, is the distance from the middle of the solid to the center of the hexagon. The same process is done using the new center of the tetrakaidecahedron. The result is a set of two tetrakaidecahedra that itself can fill space by translation along X, Y and Z axes.

To determine if a specific atom is located inside the tetrakaidecahedron, we first determine its directed distance from the center of the solid. This can be done easily because we know the position of both the center of the solid and the atom. There are seven directed distances that we are interested in. Four correspond to the 4 squares, and the other 3 correspond to the hexagons. We need only check 3 hexagons because they are coupled with one another, in that they are parallel to each other and on opposite sides of the center of the tetrakaidecahedron. If each of the directed distances are less than their corresponding radius (either r4 or r6), then the atom is located inside the tetrakaidecahedron and it is flagged. For the open-celled configurations, the faces between the pores were removed in a similar manner.

Before testing, each configuration was allowed to relax to take its lowest energy shape. We relaxed the structure within 5% of its original size on our first attempt and if needed we extend this region. To relax the structure the size of its containing box was adjusted and let to equilibrate for 500 time steps. The configuration with the lowest average energy was assumed to be the relaxed state. Figure 9 shows the energies of several configurations.

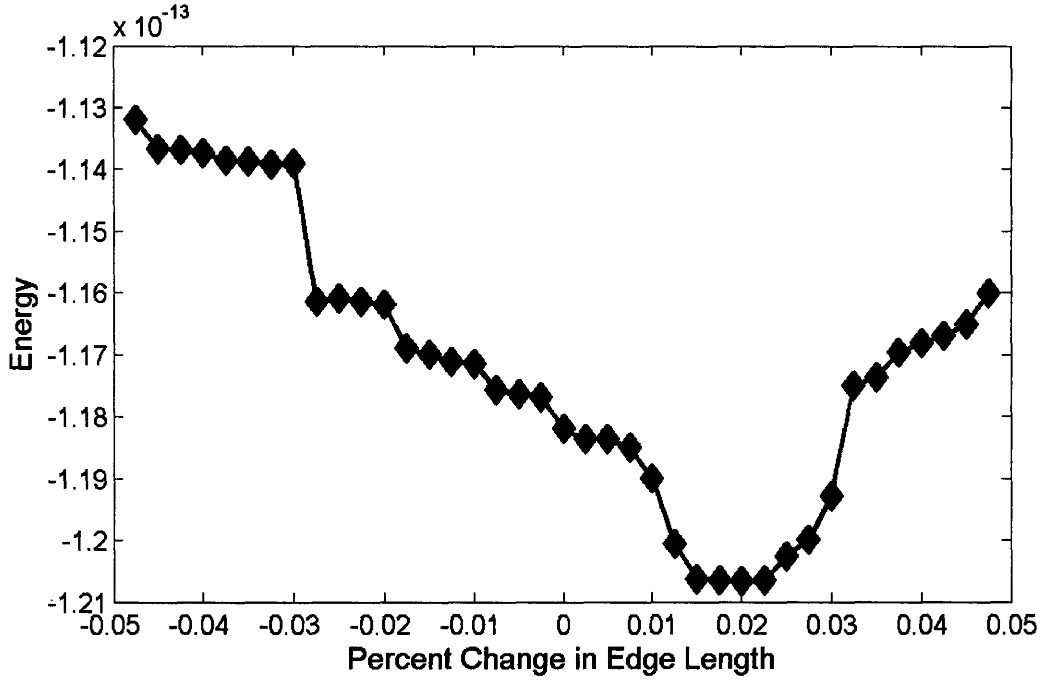

**Figure 9** Graph showing the time-averaged energy (in Joules) of the starting configuration, varying the edge length of the containing box. The minimum energy state, here at a 0.02% increased edge length, is taken as the starting configuration.

There were two types of simulations performed on the nano-porous copper foams. The first type was a time-averaged run at a given temperature, number of atoms, and volume, to determine the thermodynamic equilibrium, used to determine the starting configuration. The second type allowed for real-time deformation. In order to simulate real-time deformation we updated the cubic side length at every time step. The change in side length was determined by the strain rate:

$$\varepsilon' = \frac{\Delta l}{l * \Delta t} \tag{13}$$

Therefore,

$$\Delta l = \varepsilon' * \Delta t * l \tag{14}$$

where ε' is the strain rate, Δt is the time step, l is the cube length, and Δl is the cube length increment. For each run ε' was held constant at $10^9$.

To determine what configuration to use for our simulations we tested for convergence using 2x1x1, 4x1x1, 2x2x1, and 2x2x2 configurations. To clarify, the AxBxC convention represents the number of unit tetrakaidecahedra (shown in Figure 2) along each of the X, Y, and Z axes respectively. Thus a 2x1x1 configuration is composed of 2 tetrakaidecahedra along the x-axis and 1 in each of the other directions.

What we mean when we refer to convergence, is the relation that our smaller simulations have to larger ones. Ideally we could represent the tetrakaidecahedron foam as the one unit cell shown in Figure 2. This would reduce the number of particles in the simulation and therefore reduce the computational time. Unfortunately, if we only look at one unit cell, we do not collect data on the interaction between these cells. So how small of a configuration can we use and still see the proper sequence of events? To determine which starting configuration we using we look at the relation of the different configurations to one another. Figure 10 shows this relation, under uniaxial tension along the X-axis (to the right and left).

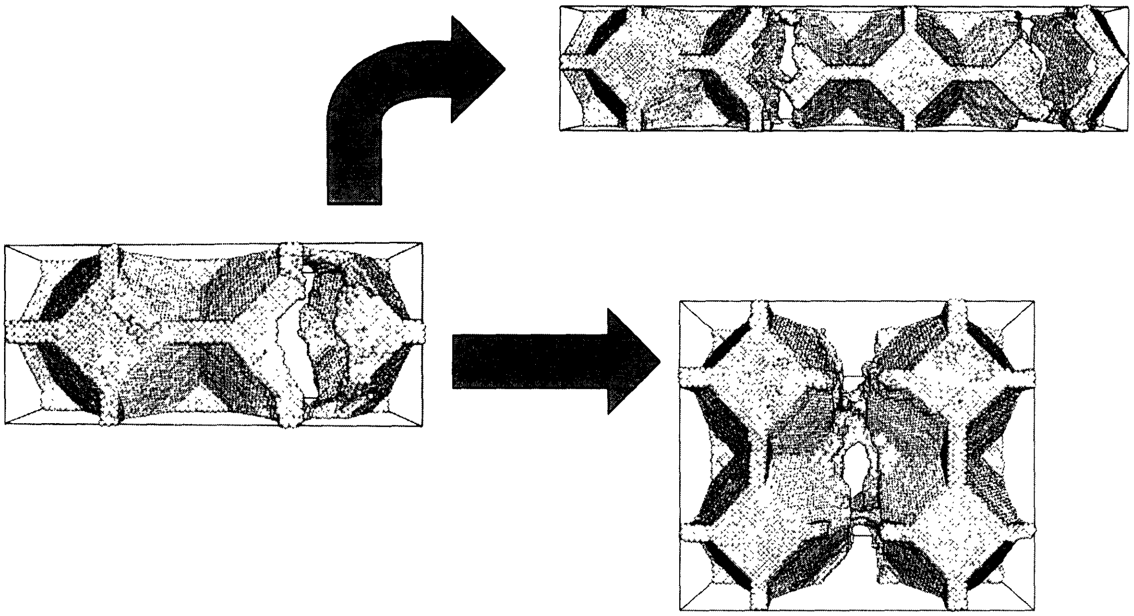

**Figure 10** Schematic showing convergence between 2x1x1 and 2x2x2 structures and non-convergence between 2x1x1 and 4x1x1 structures. The non-convergence is an artifact of how strain is applied to the system.

We notice that in the 2x1x1 configuration, we see the propagation of 1 crack. The crack runs through the center of one of the unit tetrakaidecahedron. We suspect that if we increase the simulation from 2x1x1 to 4x1x1 we would still only have 1 crack. Unfortunately, the 4x1x1 has the propagation of 2 cracks.

The creation of the second crack is an artifact of how we deform the structure. It is important to note, we do not apply stress to the structure. Instead, we apply a constant strain. The strain is applied by increasing the appropriate edge length. This immediately affects the distances between all the atoms, which usually equilibrates during the time step, and under most circumstances acts as if we had applied stress directly to the system. It is possible, however, the strain is distributed between 2 cracks, causing both to propagate, seen in Figure 10.

It appears, from Figure 10, the 2x1x1 foam shows convergence and therefore we could have used this structure or any larger translation of it for our testing. To understand more about the system it is optimal to have the greatest possible area for the plane perpendicular to the strain axis, and for this reason, simulations were run using the 2x2x2 structure.

# Chapter 4

## Results and Discussion

Because we performed MD simulations and thus have information about every atom, we use AtomEye [Li, 2003] to help us visualize our simulations. With AtomEye we can see what macro-scale failure mechanisms occur, Figure 11, and atomistic mechanism, Figure 12.

Figure 11 is colored based on atom displacement. The coloring scheme is changing throughout the pictures so that red represents atoms with the largest displacement and dark blue represents the atoms with the least displacement. By examining Figure 11, we can see that our foam undergoes all the proper stages of metallic foam deformation. At point *(a.)*, we are in the elastic regime with the strain being evenly distributed throughout the structure. We see this because the patches of light blue appear to be even throughout the structure. By point *(b.)*, we notice that there is a localization of the strain located in the upper right part of the picture. This suggests a type of plastic deformation has occurred. At *(c.)*, the structure has begun to fracture. The strain localizes around the crack and larger displacements occur in that region. This results in the strip of red along the right side. At *(d.)*, the strain localization has caused the crack to propagate until finally we have full fracture at *(e.)*.

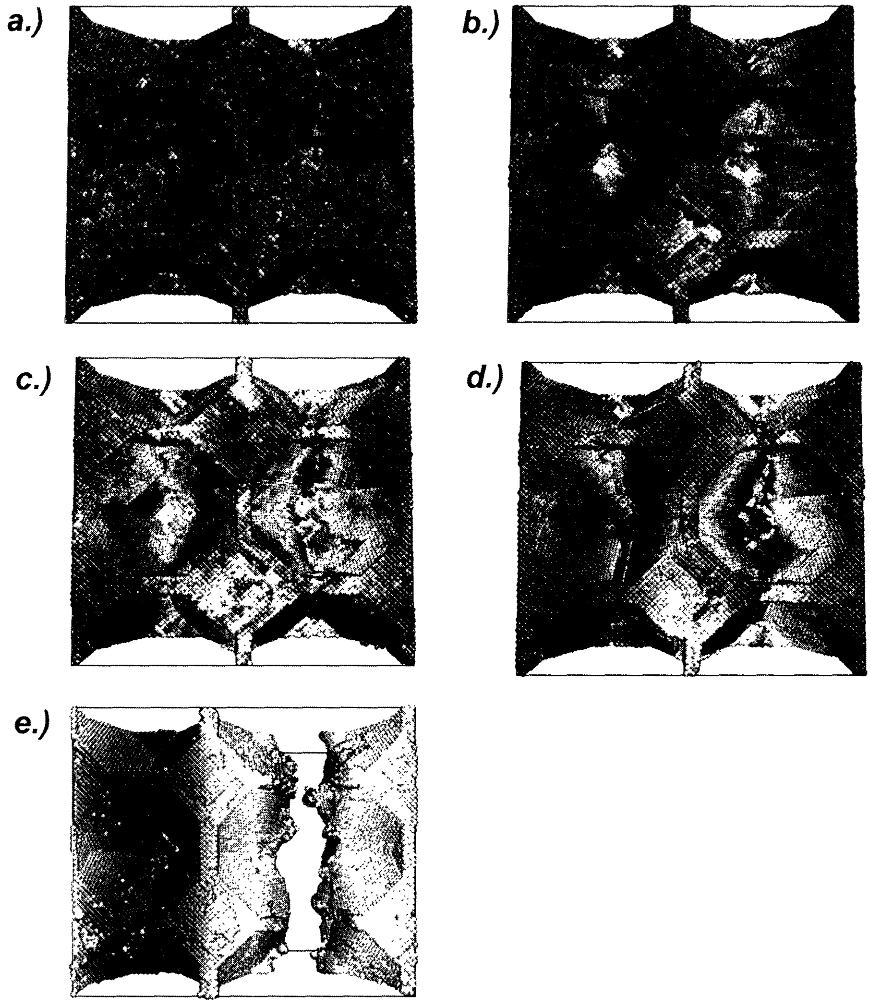

**Figure 11** Series of figures representing the continuum properties of a metal foam. At point a.) elastic regime, b.) onset of plastic deformation, c.) nucleation of crack, d.) crack propagation, e.) full fracture.

This behavior fits very well with what is seen in macro-scale metallic foams. Furthermore, it is interesting to note here is that in *(b.)* there appears to be two locations where the strain is localized. It appears that the strain on the right "wins" and thus the fracture is formed there. We see also that after the crack is nucleated and begins to propagate through *(d.)*, the left side of the structure appears to return to a low stress state. This would be expected because cracks are stress concentrators and the creation of a crack relieves the global stress.

By examining the same simulation with a different color scheme, we can examine what occurs before, during and after the fracture at the atomistic level. Figure 12 is colored by oordination number. Coordination number is an atom's number of nearest neighbors. In an FCC crystalline structure the coordination number of all atoms would be 12, which is the tan color in Figure 12. The purple and gray colors represent FCC surfaces, in the <111> and <100> planes respectively.

In Figure 12 at *(a.)*, we see the elastic regime. Most of the atoms are in their correct coordination number and those that are not are evenly distributed throughout the structure. By *(b.)*, there exists some plastic deformation. A partial dislocation appears to have moved along the <111> plane just to the right of the left strut. There also appear to be several dislocations in all of the FCC faces. By *(c.)*, a crack has formed and at *(d.)* the crack propagates through the faces. As the crack propagates, partial dislocations seem to disperse out from it. At the same time, the partial dislocations appear to be leaving the right side of the structure. By *(e.)* the crack has almost fully propagated. As it does so, a slew of edge dislocations form to the left of the strut. By *(f.)* the fracture is almost complete, and the remainder of the system begins to return to its minimal energy state.

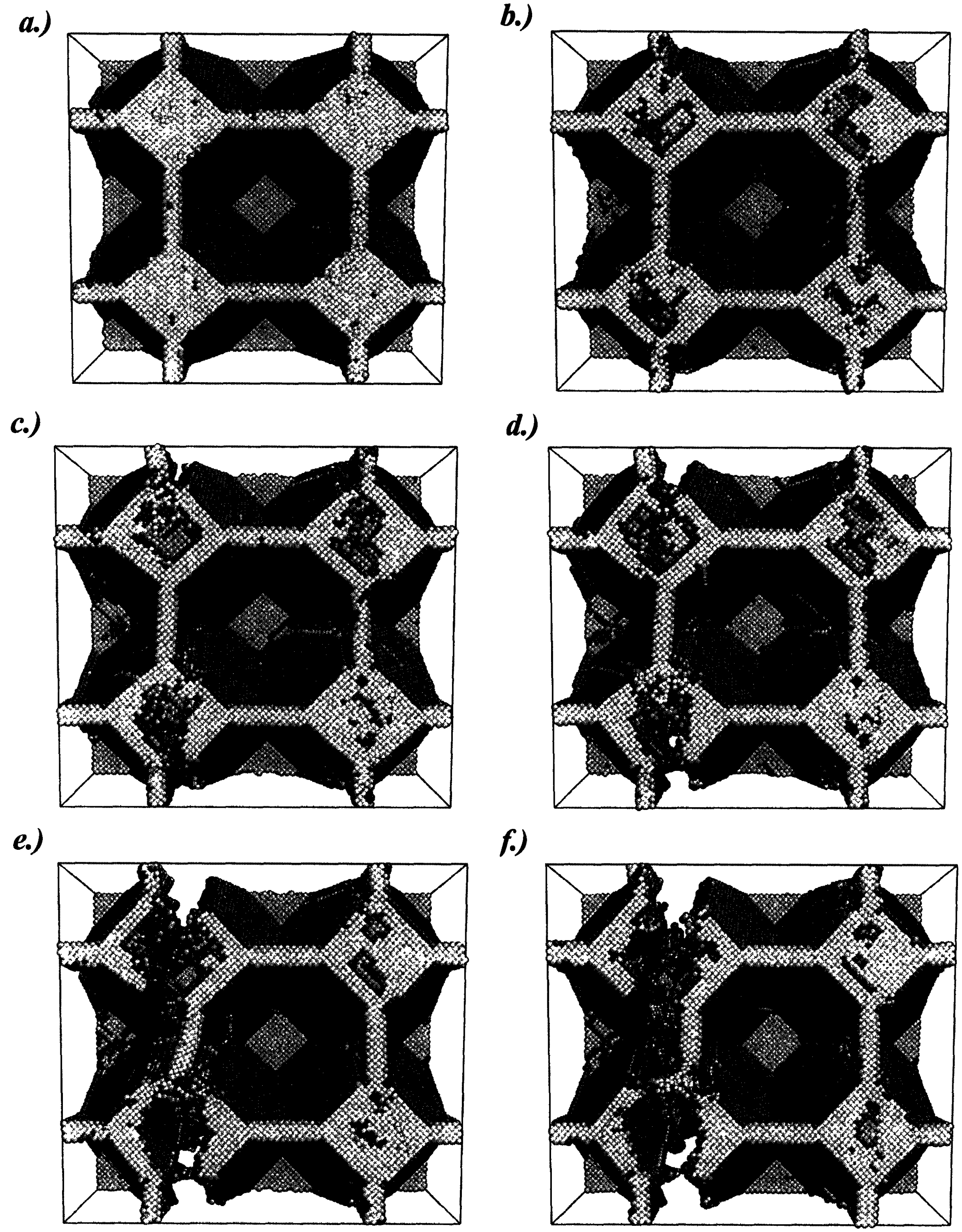

**Figure 12** Series of figures representing the atomistic properties of metal foams. Figures are colored using coordination number and progress in time. The system begins in a relaxed state and ends as a nearly fully fractured structure.

Stress-strain curves for structures of the same density are shown in Figure 13. The three curves vary only in pore size, from 60,000 to 200,000 atoms maintaining a constant pore to strut ratio.

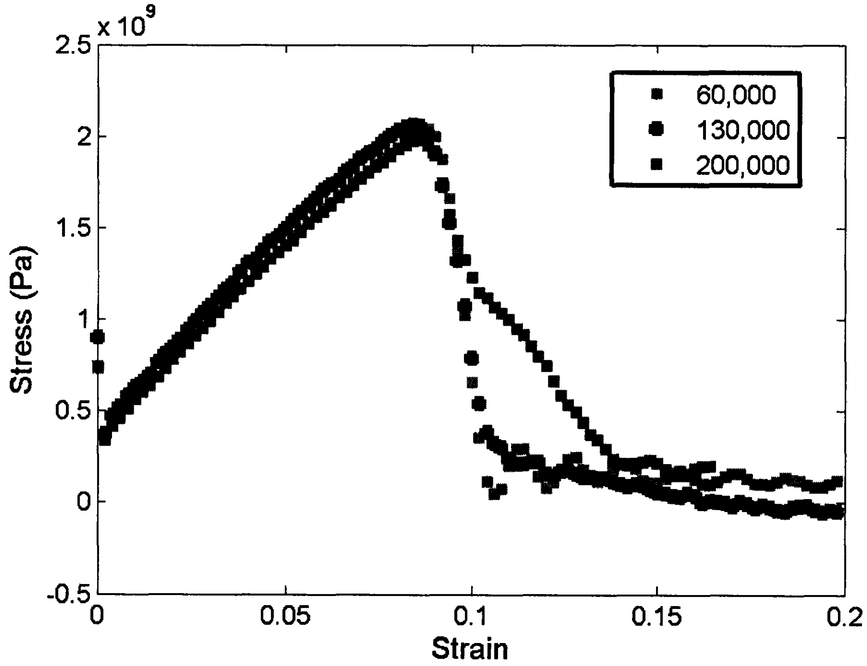

**Figure 13** Plot of the stress-strain curves for a series of simulations varying only the size of the simulation (shown in the legend). All simulations have similar yield stresses and Young's moduli but appear to have slightly different behavior following crack formation

These stress-strain curves have many of the same characteristics that a theoretical macro-scale metallic foam would have. They have the elastic regime, the onset of plastic deformation, crack nucleation and full fracture. These stress-strain curves lack an important regime, however. They do not appear to have the elongated crack propagation section (described by *(d.)* in Figure 5).

Interestingly, the three simulations have roughly the same yield stresses and the same Young's moduli. However, the three appear to have slightly different behavior following initial fracture. The largest simulation dislplays a hump in the curve following the initial fracture. It appears that this would be the beginning of the fracture propagation regime in the theoretical stress-strain curve. Figure 14 shows visualizations of the above simulations at a strain of approximately 12%. In the smaller simulation, the crack almost immediately fully propagates through the structure. Though it is difficult to see in the picture the crack has propagated through in a jagged manner, and only 2 small struts hold the sides together. In the larger simulation, the crack has only begun to propagate through the structure at 12% strain. This would suggest that as we further increase the number of particles, the propagation step should elongate, eventually looking like the theoretical stress-strain curve.

There are two possible explanations for the absence of the propagation region. First, we simulated a small structure that has only 2 pores along the y-axis (the axis along which the crack propagates). This means the crack can only propagate for a short period of time before it fully fractures the structure. We would expect that as the number of pores along the y-axis increases, a zippering effect would exist and thus the propagation regime would elongate. Secondly, as the number of particles increases the energy required for the crack to propagate should increase; thus, the propagation regime should elongate which explains the hump we see in Figure 13.

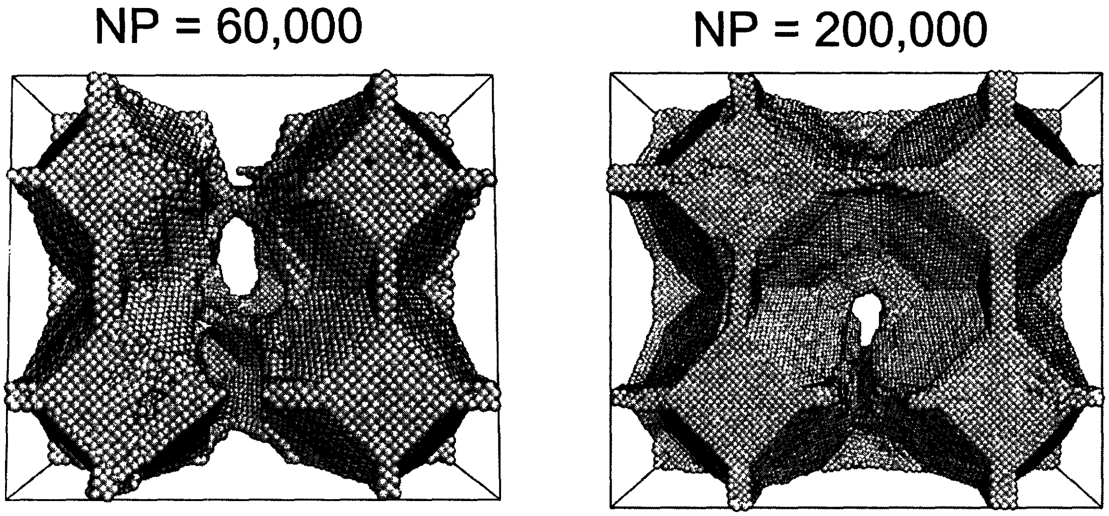

**Figure 14** Atomistic representations of the simulations shown in Figure 11 at a strain of 12%. The only difference between the 2 simulations is the number of particles. In the smaller simulation there is almost full fracture.

From the stress-strain curves the Young's moduli and yield stresses can be determined for our simulations. We compare our simulated data to the quasi-linear constitutive theory in for the relative Young's modulus in Figure 15 and for the relative yield stress in Figure 16.

The simulated Young's moduli appear to correlate very well with current theory. This correlation intuitively makes sense because the Young's modulus of a structure relates strongly with the potential used. Since the simulations were run with the very accurate Mishin potential, the Young's moduli should match well with theory.

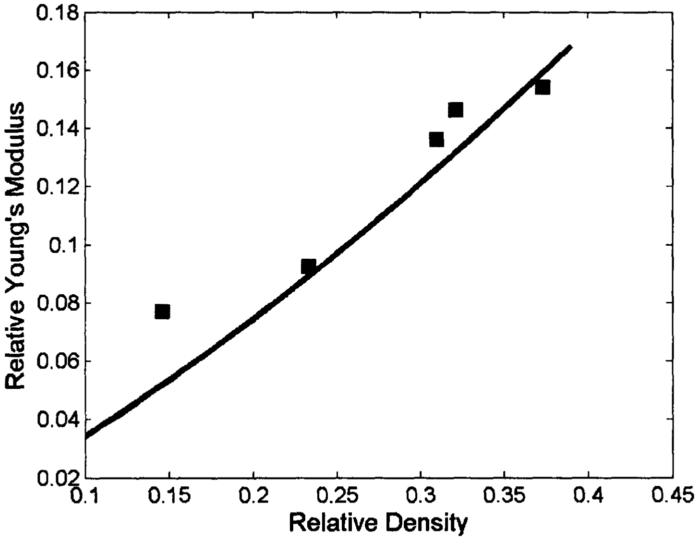

**Figure 15** Graph of the theoretical Young's Modulus to relative density vs. data collected from simulations varying. Simulated results match very closely to constitutive theory.

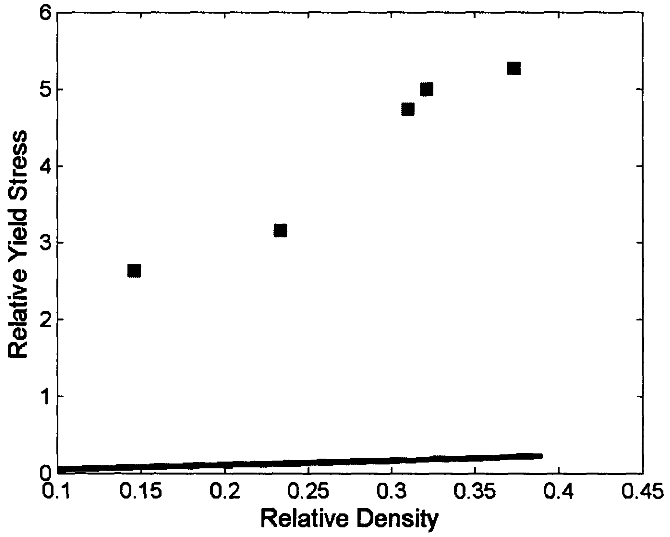

**Figure 16** Graph of the theoretical Yield Stress to relative density vs. data collected from simulations. Simulated results are approximately 1 order of magnitude above constitutive theory.

There is, however, a drastically different relation between the simulated yield stresses and the theoretical yield stresses, approximately an order of magnitude difference. There are several explanations for this discrepancy. First, to determine the relative yield stress the experimental yield stress of solid copper, 130 MPa [Gibson 2000], was used. The experimental yield stress was determined using a strain rate on the order of $10^{-3}$, so it is hard to compare the two yield stresses. Furthermore, the simulation was performed with a very large strain rate of $10^{9}$. Large strain-rates are known to stress systems past their theoretical maximum yield stresses by not allowing structures to adequately relax.

To examine this situation further we determined the yield stress of a perfect FCC crystalline copper structure using a strain rate of $10^{9}$. The resulting yield stress, 11 GPa, is approximately 2 orders of magnitude higher than experimental results. Using the resulting yield stress as the yield stress of solid copper, the relative yield stress dropped dramatically, shown in Figure 17.

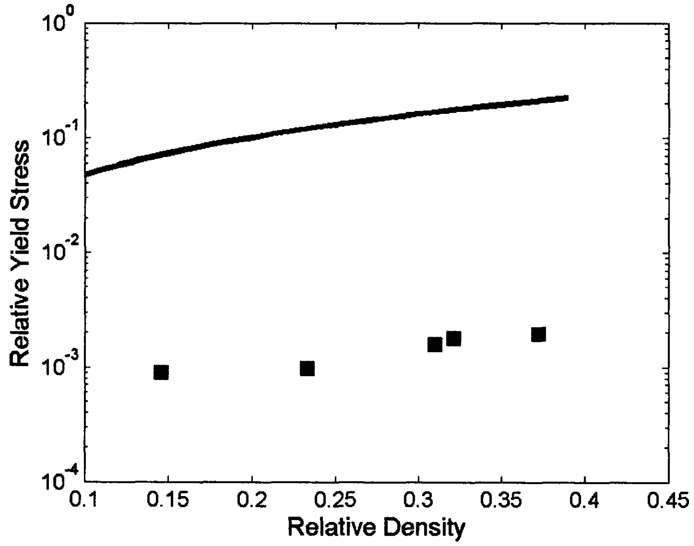

**Figure 17** Graph of the theoretical Yield Stress to relative density vs. data collected from simulations using the yield stress for a perfect FCC crystal. Simulated results are approximately 1 order of magnitude below constitutive theory.

In each case, the simulated relative yield stresses are off by approximately 1 order of magnitude. This is most likely due the high strain rate. The constitutive theory describes a regime under a much slower strain rate. The data suggest the increased strain rate affects the foam to a greater extent than the solid, which is why the data do not match properly in the Figure 17.

# Chapter 5

## Further Results

As additional work we attempted to validate the constitutive theory of open-celled foams at the nano-scale. To do this, we ran simulations varying porosity from 0.14 to 0.37 on our open-celled foams. Unfortunately, the data was not intuitively correct. As a result, we were unable to draw any concrete conclusions from the open-cell simulations.

The open-celled foams displayed almost fluid-like under tension and compression. Figure 18 shows the open-celled foam under tensile strain and Figure 19 shows the foam under compression. Both figures are colored according to atomic displacement, using a variable colorbar.

Under tension, typical metallic foams should under go elastic deformation and eventually plastic deformation will occur. The open-cell foam simulations did in fact display these regimes, however, beyond the initial fracture the foam like properties disappeared. In Figure 18, at point *(a.)* the foam appears to be in the elastic regime and at *(b.)* the strain has localized in the upper right strut. Eventually, by *(d.)* the strut breaks and as before there is an initial fracture. After the initial fracture, the broken struts should remain solid, however, in the simulation (Figure 18 *(e.)* and *(f.)*) the struts coalesce with one another to form a larger strut. This phenomenon is not solid-like but rather more fluid-like. Further in the simulation, not shown in Figure 18, more coalescence occurs. Because of the combining of struts, the simulations do not represent metallic foams and thus can not be compared to constitutive theory.

Interestingly, the open-celled foam acted "fluid-like" under compressive strain as well. Figure 19 shows a series of pictures of the foam in compression. Under compression, the pores in typical metallic foams would collapse abruptly. The simulated foams, rather, mush together with no abrupt collapsing of the pores. From figure *(a.)* to figure *(e.)* little happens plastically. The pores simply get smaller at a nearly constant rate. This behavior is more "fluid-like" because the foam is simply molding to fit inside the confining box.

There are several possible explanations as to why the open-cell foam behaves in a "fluid-like" manner. First, it is possible the struts are simply too small (roughly 4 atoms in diameter), to act in a solid manner. Secondly and more likely, the open-cell foam is semi-stable. As an artifact of how the foam was created, the cross-sections of the struts are not square or circular but rather pentagonal. This is physically unlikely and causes the foam to want to reshape its struts. The resulting semi-stable configuration is more likely to reduce energy through coalescing with itself.

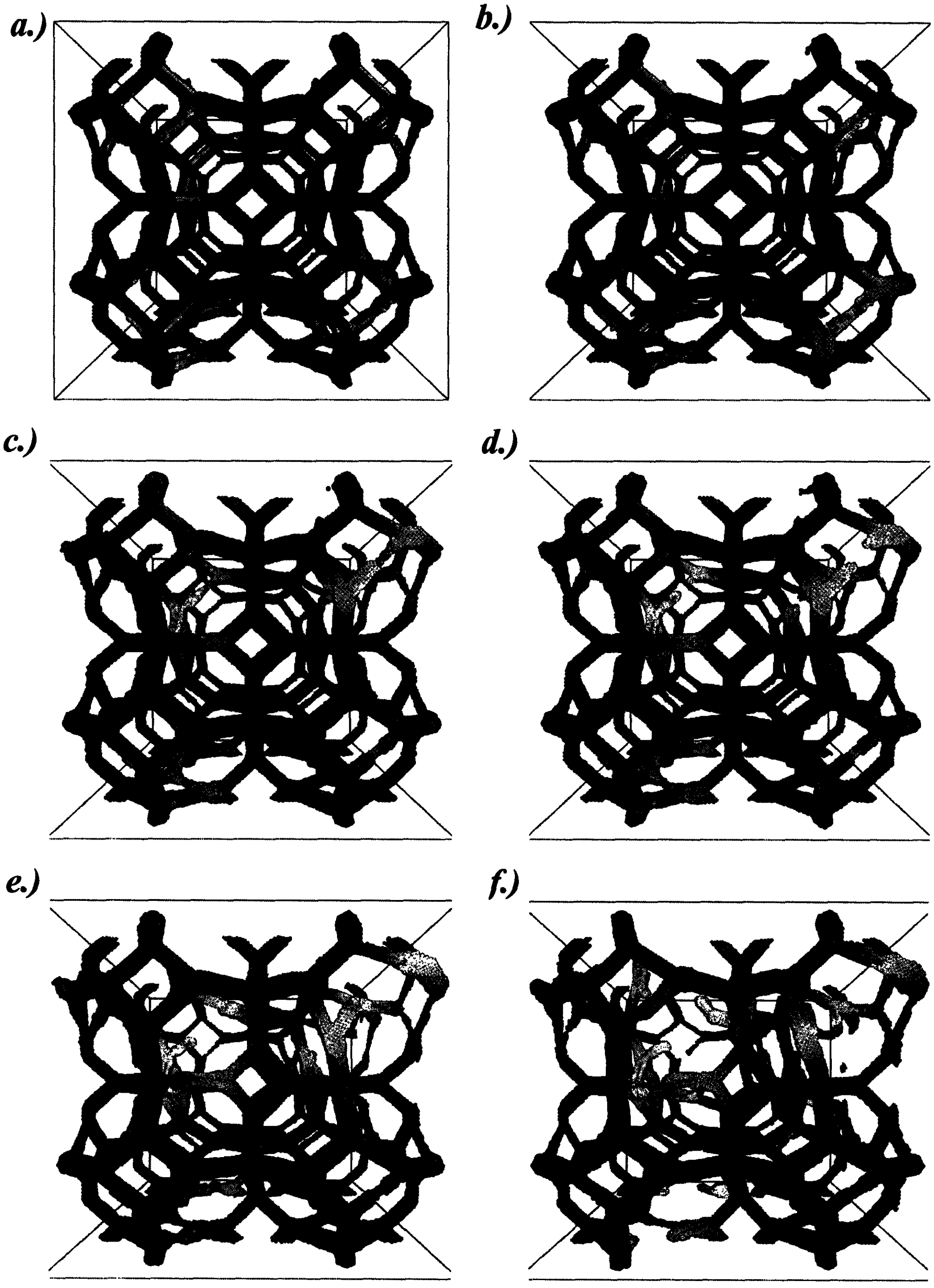

**Figure 18** Series of figures representing the continuum properties of a metal foam under tension. At point a.) elastic regime, b.) localization of strain, c.) breaking of strut, d.) full fracture of strut, e.) and f.) fusion of two struts.

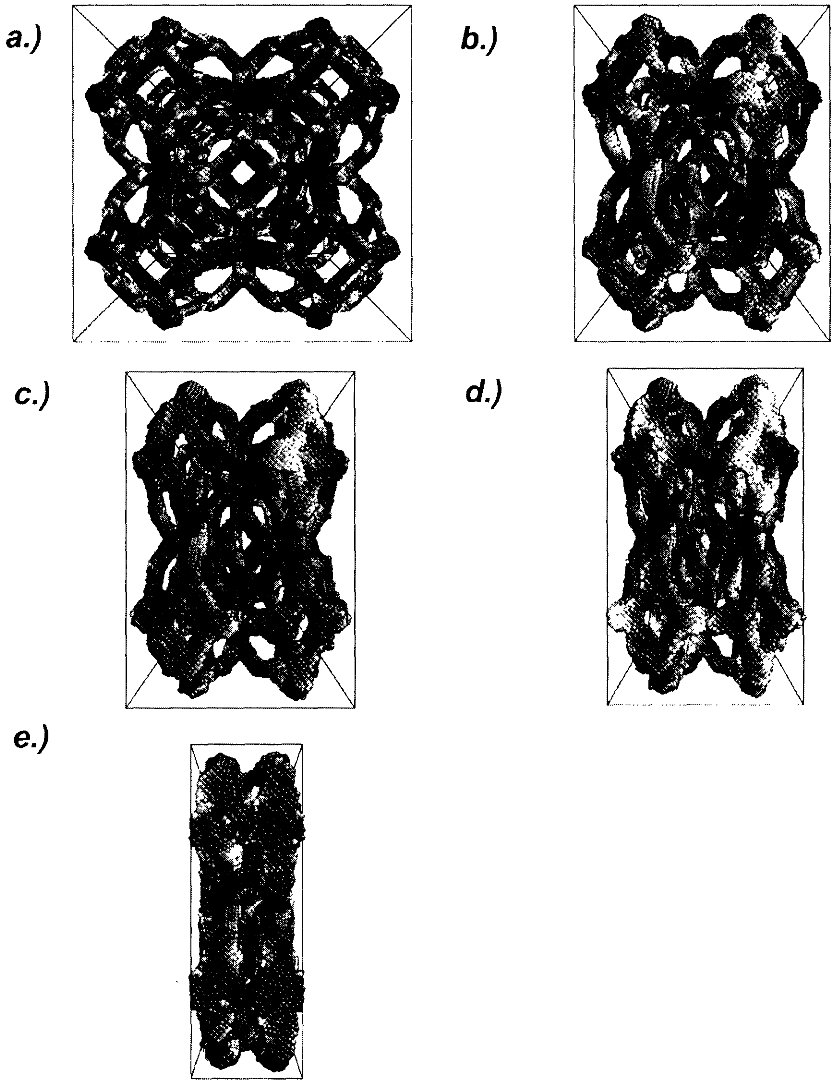

**Figure 19** Series of figures representing the continuum properties of a metal foam under compression. At point a.) elastic regime, b.) onset of plastic deformation, c.) removal of pore, d.) fewer pores, e.) approaching full compression.

# Chapter 6

## Conclusions

To determine if macro-scale metallic foam theory scaled appropriately to nanoporous foams, the mechanical behavior of nanoporous copper was simulated using molecular dynamics. Foams were created using a tetrakaidecahedron foam structure and deformed at a constant strain rate of $10^9$. Simulations were run at a constant temperature of 300° K using velocity rescaling and results were visualized using AtomEye.

The results presented suggest the constitutive theory scales well to closed-celled nanoporous foams. Our foams showed proper failure mechanisms. They progressed from the elastic regime into the onset of plastic deformation and following crack nucleation there was the beginning of crack propagation and finally full fracture. The stress vs. strain curves appeared to be approaching those of macro-scale foams and the Young's moduli fit current foam theory.

# Bibliography

E.W. Andrews and L.J. Gibson, "On notch-strengthening and crack tip deformation in cellular metals", *Mat. Letters.* **57** (2002) 532-536.

E.W. Andrews and L.J. Gibson, "The Influence of Crack-Like Defects on the Tensile Strength of an Open-Cell Aluminum Foam", *Scripta Mater.* **44** (2001) 1005-1010.

E.W. Andrews and L.J. Gibson, "The role of cellular structure in creep of two-dimensional cellular solids", *Mat. Sci. Eng.* **A303** (2001) 120-126.

E.W. Andrews, J.S. Huang, and L.J. Gibson, "Creep Behavior of a Closed-Cell Aluminum Foam", *Acta Mater.* **47** (1999) 2927-2935.

E. Andrews, W. Sanders, and L.J. Gibson, "Compressive and tensile behaviour of aluminum foams", *Mat. Sci. Eng.* **A270** (1999) 113-124.

J. Biener, A. M. Hodge, and A. V. Hamza, "Microscopic failure behavior of nanoporous gold", *Appl. Phys. Letters* **87** 121908 (2005).

J. Biener, A. M. Hodge, A. V. Hamza, L. M. Hsiung, and J. H. Satcher, "Nanoporous Au: A high yield strength material", *J. Appl. Phys.* **97** 024301 (2005).

R.D. Boyer, J. Li, S. Ogata, and S. Yip, "Analysis of shear deformations in Al and Cu: empirical potentials versus density functional theory", *Modelling Simul. Mater. Sci. Eng.* **12** (2004) 1017-1029.

A. H. Brothers and D. C. Dunand, "Plasticity and damage in cellular amorphous metals", *Acta Mater.* **53** (2005) 4427-4440.

G. Cailletaud, S. Forest, D. Jeulin, F. Feyel, I. Galliet, V. Mounoury, and S. Quilici, "Some elements of microstructural mechanics", *Computational Mat. Sci.* **27** (2003) 351-374.

L.J. Gibson, "Mechanical Behavior of Metallic Foams", *Annu. Rev. Mater. Sci.* **30** (2000) 191-227

G. Gioux, T.M. McCormack, and L.J. Gibson, "Failure of aluminum foams under multiaxial loads", *Inter. J. Mech. Sci.* **42** (2000) 1097-1117.

J. L. Grenestedt and K. Tanaka, "Influence of Cell Shape Variations on Elastic Stiffness of Closed Cell Cellular Solids", *Scripta Materialia* **40** (1999) 71-77.

J. L. Grenestedt, "Effective elastic behavior of some models for 'perfect' cellular solids", *Inter. J. Solids and Struct.* **36** (1999) 1471-1501.

F. Han, H. Cheng, J. Wang, and Q. Wang, "Effect of pore combination on the mechanical properties of an open cell aluminum foam", *Scripta Mater.* **50** (2004) 13-17.

J. Li, *Modelling Simul. Mater. Sci. Eng.* **11** (2003) 173

N.J. Mills and H.X. Zhu, "The high strain compression of closed-cell polymer foams", *J. Mech. Phys. Solids.* **47** (1999) 669-695.

P.R. Onck, R. Van Merkerk, A. Raaijmakers, and J.T.M. De Hosson, "Fracture of open- and closed-cell metal foams" *J. Mat. Sci.* **40** (2005) 5821-5828.

G.E. Palmer, W.D. Henline, D.R. Olynick, and F.S. Milos, "High-Fidelity Thermal Protection System Sizing of Reusable Launch Vehicle", *J. Spacecraft and Rockets* **34** (1997) 577-584.

A.P. Roberts and E.J. Garboczi, "Elastic Moduli of Model Random Three-Dimensional Closed-Cell Cellular Solids", *Acta Mater.* **49** (2001) 189-197.

A.E. Simone and L.J. Gibson, "Effects of solid Distribution on the Stiffness and Strength of Metallic Foams", *Acta Mater.* **46** (1998) 2139-2150.

S. Yip, Lecture Notes 7 for 22.00, Introduction to Modeling and Simulation, (2000).

H.X. Zhu, J.F. Knott, and N.J. Mills, "Analysis of the Elastic Properties of Open-cell foams with Tetrakaidecahedral Cells", *J. Mech. Phys. Solids.* **45** (1997) 319-343.

H.X. Zhu and N.J. Mills, "Modelling the creep of open-cell polymer foams", *J. Mech. Phys. Solids.* **47** (1999) 1437-1457.